Available online at www.sciencedirect.com
ScienceDirect
Trans. Nonferrous Met. Soc. China 32(2022) 3222−3237
Transactions of Nonferrous Metals Society of China
www.tnmsc.cn

Microstructural evolution and mechanical performance of cast Mg−3Nd−0.2Zn−0.5Zr alloy with Y additions

He XIE[1], Guo-hua WU[1], Xiao-long ZHANG[1], Zhong-quan LI[2], Wen-cai LIU[1], Liang ZHANG[1], Bao-de SUN[1]

1. National Engineering Research Center of Light Alloy Net Forming and State Key Laboratory of Metal Matrix Composites, School of Materials Science and Engineering, Shanghai Jiao Tong University, Shanghai 200240, China;
2. Shanghai Spaceflight Precision Machinery Institute, Shanghai 201600, China

Received 19 August 2021; accepted 16 February 2022

Abstract: This work investigated the effects of different Y additions (0, 1.5, 3.0 and 4.5 wt.%) on the microstructural evolution and mechanical performance of cast Mg−3Nd−0.2Zn−0.5Zr alloy. The results show that as the Y content increases, the key secondary phases in as-cast alloys change from the $Mg_{12}Nd$ type to the $Mg_{24}Y_5$ type. Meanwhile, the number density of Zn−Zr particles in the grains of as-quenched alloys gradually decreases. HAADF-STEM observations of peak-aged samples reveal that element Y is greatly enriched in the globular β' precipitates, leading to a significantly increased volume fraction and promoted precipitation kinetics of β' precipitates, resulting in enhanced strength of the alloy. Tensile tests reveal that, with the addition of 4.5 wt.% Y, the yield strength of the base alloy is substantially increased by 88 and 61 MPa after being aged at 200 and 225 °C under peak-aged conditions, respectively.

Key words: Mg−3Nd−0.2Zn−0.5Zr alloy; Y alloying; age-hardening response; microstructural evolution; mechanical properties

1 Introduction

The last decades have seen a growing trend towards developing cast rare-earth (RE) containing magnesium alloys due to their great potential for forming large complex thin-walled parts in various critical applications such as aerospace and vehicle engineering [1−3]. Among the developed cast magnesium alloys containing RE elements, Mg−Y−Nd system alloys, such as WE43 and WE54 alloys, are successful commercial as-cast magnesium alloys widely used [4−6]. As typical heat-treatable Mg-RE alloys, the excellent strength of Mg−Y−Nd alloys is mainly derived from potent solid solution strengthening and precipitation hardening effects. Precipitation strengthening is generally accepted as the most effective approach that will significantly increase the yield strength [7−10]. The strengthening effects are dominantly determined by the distribution and intrinsic properties of the precipitates. The precipitation sequence in the Mg−Y−Nd alloys has been investigated comprehensively, which gives the order of SSSS → ordered G.P. zones (zigzag shape)→ β'' ($D0_{19}$, hexagonal prism) → β' (orthorhombic, globular shape) → β_1 (fcc, $\{10\bar{1}0\}_\alpha$ plate) → β (fcc, $\{10\bar{1}0\}_\alpha$ plate) [11−13].

Recently, Y_2O_3 inclusions have been found to be readily formed in the preparation of Mg−Y−Nd alloy castings and significantly reduce the qualified rate, which is mainly attributed to the relatively high content of highly reactive Y element [14,15]. Thus, several attempts have been made to develop novel Mg−RE alloys with lower Y contents [16−18]. The existing body of research suggests that simply

Corresponding author: Guo-hua WU, Tel: +86-21-54742630, E-mail: ghwu@sjtu.edu.cn;
Xiao-long ZHANG, Tel: +86-15821905395, E-mail: XLZhang1993@sjtu.edu.cn
DOI: 10.1016/S1003-6326(22)66015-1

lowering the Y content will significantly deteriorate the strength of Mg−Y−Nd alloys [16]. It is worth noting that replacing Y with Gd might be a potentially feasible approach. As previously reported, by replacing part of Y with Gd accompanied by the unchanged total rare earth content, the Mg−2Y−3Gd−2Nd alloy exhibits the same mechanical properties as the Mg−4Y−1Gd−2Nd alloy at ambient and elevated temperatures [16]. However, previously published studies are mainly limited to the influence of the Gd/Y ratio on the mechanical properties of Mg−Nd alloys. The main practical problem that confronts us is why Gd can replace the Y element in Mg−Y−Nd system alloys. It is of great significance to investigate the separate roles of Gd and Y in the microstructure evolution, especially the precipitation behavior of Mg−Nd alloys. In our recent work, we have investigated the influence of Gd content on the microstructures and mechanical properties of Mg−3Nd−0.2Zn−0.5Zr alloy [17]. Gd additions resulted in significant strength improvement due to the significantly enhanced precipitation kinetics and strongly increased volume fraction of β'' precipitates. Nevertheless, there has been no detailed investigation of the effect of different Y contents on the precipitation behavior of Mg−Nd alloys.

Thus, the primary aim of this work is to reveal the special role of different Y contents (0, 1.5, 3.0 and 4.5 wt.%) on the microstructure and mechanical performance of cast Mg−3Nd−xY−0.2Zn−0.5Zr alloy. The precipitate microstructures of peak-aged alloys isothermally aged at 200 and 225 °C are carefully characterized by high-angle annular dark-field scanning transmission electron microscopy (HAADF-STEM). The microstructural evolution and mechanical properties of studied alloys are provided to discern the strengthening effect of the Y content in as-cast Mg−3Nd−0.2Zn−0.5Zr alloy.

2 Experimental

2.1 Materials and heat treatment

The investigated alloys in this study were prepared by conventional gravity casting, and the details of preparing the alloy were consistent with those described in our previous work [17,19]. For brevity, four investigated alloys were designated as the 0Y, 1.5Y, 3.0Y and 4.5Y alloys. The actual chemical compositions of alloys were presented in Table 1. Blocks with dimensions of 15 mm × 15 mm × 15 mm were machined from the as-cast ingots to measure the density of the studied alloys (g/cm^3) using the standard Archimedes method. All the prepared ingots were solution-treated (535 °C and 8 h for 0Y and 1.5Y alloys, and 525 °C and 8 h for 3.0Y and 4.5Y alloys), quenched into water, and subsequently aged at 200 and 225 °C for various time.

Table 1 Actual chemical compositions of as-cast alloys investigated in this work (wt.%)

Alloy	Y	Nd	Zn	Zr	Mg
0Y	−	3.05	0.25	0.46	Bal.
1.5Y	1.48	3.10	0.27	0.48	Bal.
3.0Y	3.01	3.09	0.27	0.51	Bal.
4.5Y	4.65	3.04	0.26	0.52	Bal.

2.2 Microstructure characterization

The microstructures of as-cast and as-quenched alloys were characterized by optical microscope (OM, Zeiss Axio observer) and scanning electron microscope (SEM, Phenom XL). Before the SEM observation, all samples were mechanically ground carefully, polished, and eventually etched using a picric acid solution. The peak-aged microstructure characterization was conducted using an FEI Talos F200X TEM apparatus operating at 200 kV. For TEM observations, thin foils (3 mm in diameter and 60 mm in thickness) were cut from peak-aged samples and thinned by mechanical grinding and subsequent ion milling.

2.3 Mechanical test

Vickers hardness tests were conducted on samples aged for various time by using a load of 50 N and a maintaining time of 10 s. Tensile samples were tested under a constant strain rate of 5×10^{-4} s^{-1} on a Zwick/Roell Z100 test machine.

3 Results

3.1 As-cast and as-quenched microstructures

Figure 1 shows the microstructures of as-cast alloys. As-cast alloys are composed of α-Mg matrix and secondary compounds distributed along grain boundaries. Based on the measured average grain

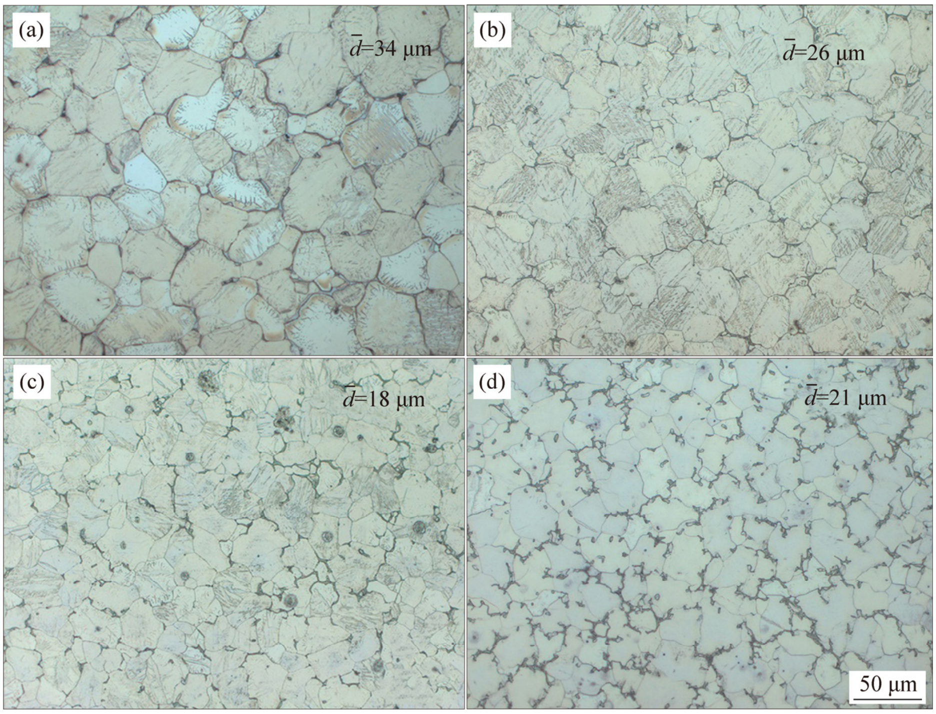

Fig. 1 OM images illustrating microstructures of as-cast alloys: (a) 0Y alloy; (b) 1.5Y alloy; (c) 3.0Y alloy; (d) 4.5Y alloy

sizes inserted in Fig. 1, increasing Y addition leads to the significant grain refinement. The average grain sizes of the as-cast 0Y, 1.5Y, 3.0Y and 4.5Y alloys are approximately 34, 26, 18 and 21 μm, respectively. Figure 2 shows the density variation of as-cast alloys with various Y contents, and it is noticeable that the increasing Y addition gradually increases the alloy density. Additionally, according to the XRD pattern of as-cast alloys (Fig. 3(a)), the dominant secondary phases in the as-cast 0Y alloy are $Mg_{12}Nd$. As the Y content increases, the diffraction peaks associated with $Mg_{12}Nd$ gradually disappear. Instead, characteristic diffraction peaks related to $Mg_{24}Y_5$-type phases are found in as-cast Y-containing alloys. For the as-cast 3.0Y and 4.5Y alloys, the main secondary phases are $Mg_{24}Y_5$-type phases.

Figure 4 shows the OM micrographs of as-quenched alloys. The averaged grain sizes of as-quenched alloys are approximately 35, 27, 24 and 29 μm, respectively. After solution treatment, most of the secondary phases distributed along grain boundaries of the as-cast 0Y and 1.5Y alloys are dissolved into the Mg matrix. In the as-quenched 3.0Y and 4.5Y alloys, sparsely uneven distribution of residual eutectic phases is observed at the triple points of grain boundaries. The phase

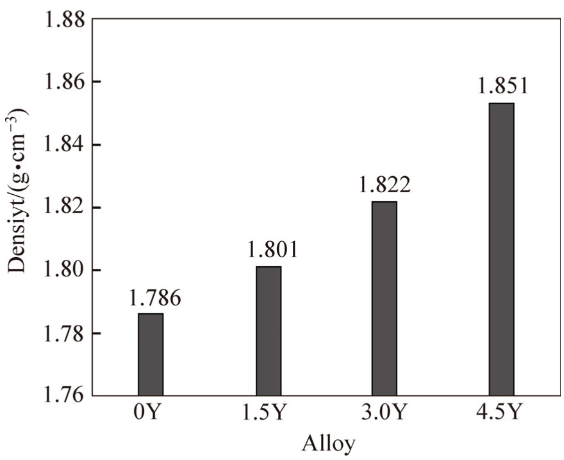

Fig. 2 Measured density of as-cast alloys

identification of as-quenched alloys in Fig. 3(b) confirms the dissolution of pre-existing eutectic phases in 0Y, 1.5Y and 3.0Y alloys, while diffraction peaks related to $Mg_{24}Y_5$-type phases are still discernible in the 4.5Y alloy.

Figure 5 exhibits SEM images of as-quenched alloys. Some rosette-like patches are visible in the grains of the as-quenched 0Y alloy, which is consistent with the Zn−Zr particles reported previously in studies on Mg−Nd−Zn−Zr alloys [19,20]. It is noteworthy that the number density of these Zn−Zr particles gradually decreases with increasing Y content.

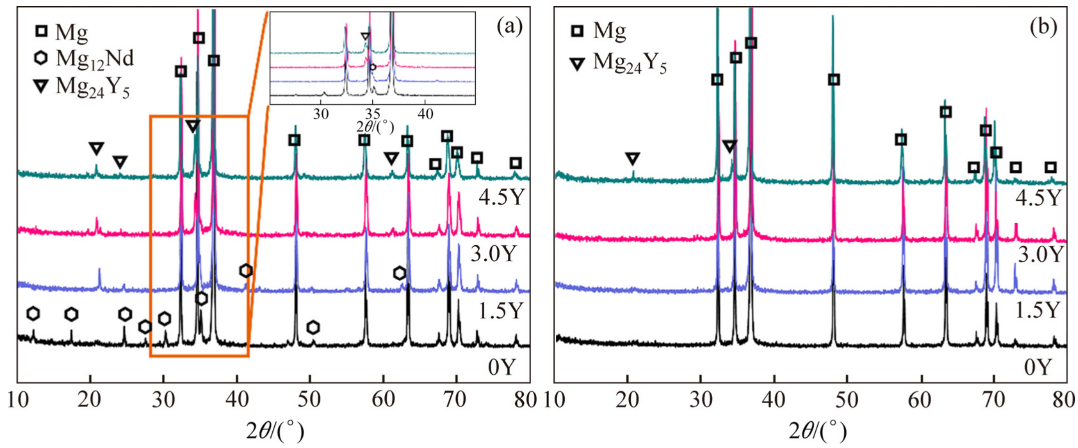

Fig. 3 XRD patterns of as-cast (a) and as-quenched (b) alloys

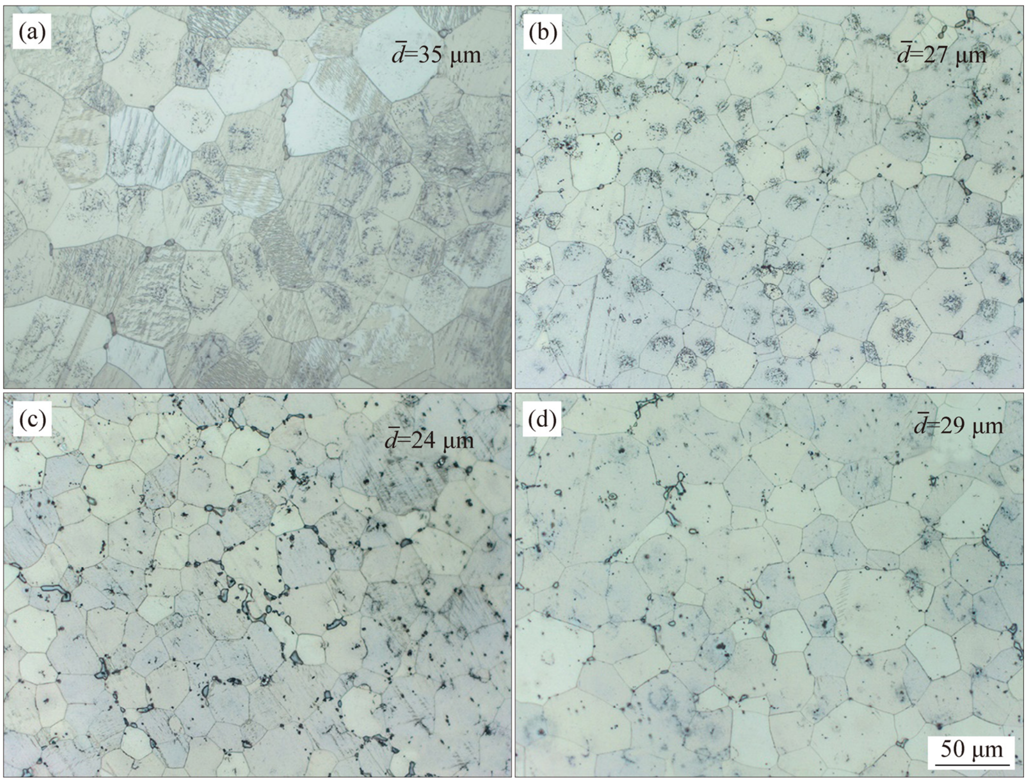

Fig. 4 OM micrographs showing microstructures of as-quenched alloys: (a) 0Y alloy; (b) 1.5Y alloy; (c) 3.0Y alloy; (d) 4.5Y alloy

3.2 Age-hardening responses

Figure 6 compares the hardness curves of alloys isothermally aged at 200 and 225 °C. The critical characteristics of age-hardening curves are listed in Table 2. In the as-quenched condition, when Y content is increased from 0 to 4.5 wt.%, the hardness value of alloys gradually increases from HV 49 to HV 76. As shown in Fig. 6(a), during ageing at 200 °C, the hardness of the 0Y alloy increases rapidly and reaches the peak value of HV 75 at approximately 16 h. Subsequently, the hardness decreases with the prolonged ageing time. Y additions significantly prolong the first increasing stage and concurrently produce a noticeable increment in the peak hardness. As the Y addition increases to 4.5 wt.%, the time required to reach the peak is extended from 16 h (0Y alloy) to 128 h (4.5Y alloy). The increment of peak hardness value associated with 4.5 wt.% Y is HV 45. The hardness curves of alloys isothermally aged at 225 °C are provided in Fig. 6(b). The age-hardening process has been significantly accelerated compared with

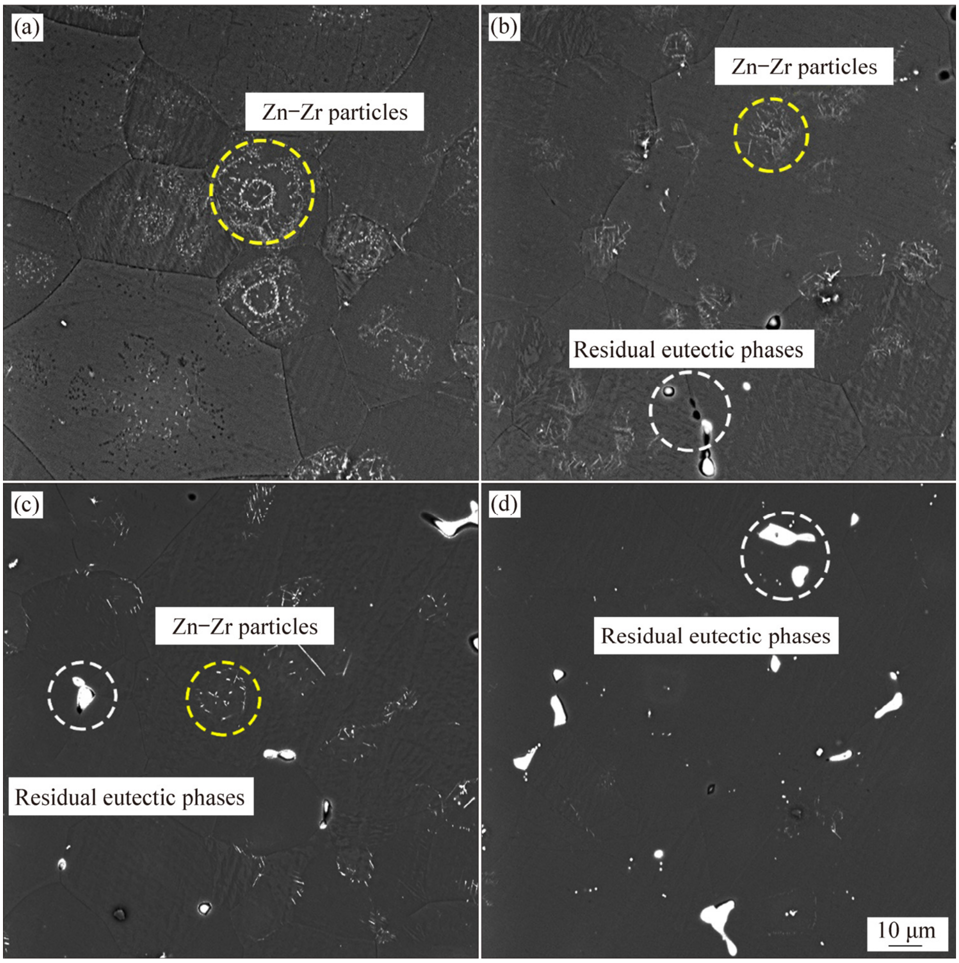

Fig. 5 SEM micrographs illustrating microstructures of as-quenched alloys: (a) 0Y alloy; (b) 1.5Y alloy; (c) 3.0Y alloy; (d) 4.5Y alloy

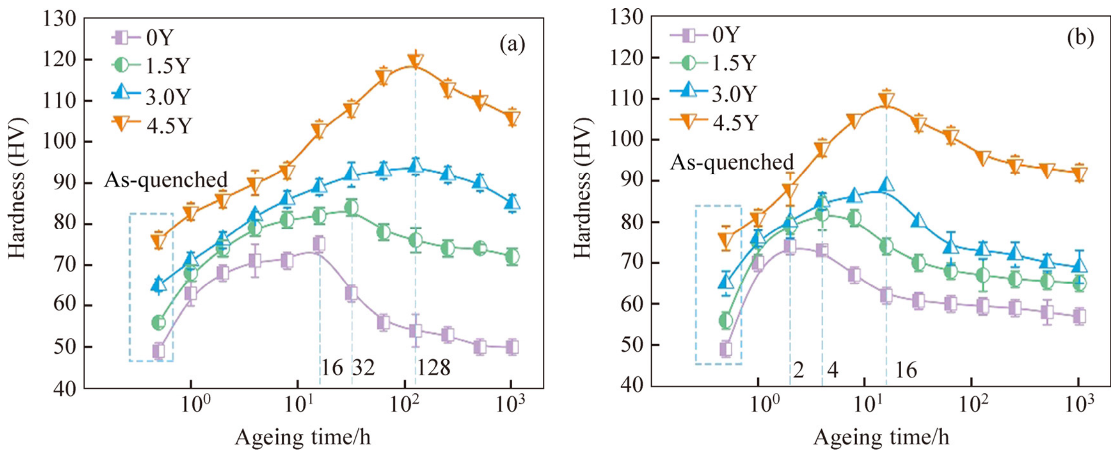

Fig. 6 Comparison of age-hardening curves of alloys obtained during isothermal ageing at 200 °C (a) and 225 °C (b)

the hardness curves in Fig. 6(a) (aged at 200 °C). The time required for alloys to reach the peak hardness is shortened dramatically from 16, 32, 128 and 128 h to 2, 4, 16 and 16 h, respectively. Meanwhile, it is noteworthy that the peak hardness values of the samples aged at 225 °C are slightly lower than those of the samples aged at 200 °C. According to these age-hardening curves, it is inferred that the additions of Y lead to significantly enhanced age-hardening responses of the 0Y alloy at the ageing temperatures of 200 and 225 °C.

Table 2 Key features of age-hardening curves

Alloy	As-quenched hardness (HV)	Aged at 200 °C		Aged at 225 °C	
		Peak hardness (HV)	Time to peak hardness/h	Peak hardness (HV)	Time to peak hardness/h
0Y	49±2	75±2	16	73 ± 1	2
1.5Y	56±1	84±2	32	82 ± 4	4
3.0Y	65±1.5	94±2	128	88 ± 0.5	16
4.5Y	76±2	120±1	128	110 ± 2	32

3.3 Peak-aged microstructure

To clarify the fundamental mechanism for the enhanced age-hardening response due to Y additions, the microstructures of peak-aged alloys are characterized as follows.

3.3.1 Peak-aged microstructure at 200 °C

Figure 7 provides HAADF-STEM and BF-STEM images illustrating the matrix precipitation of peak-aged alloys aged at 200 °C, taken with the incident beam parallel to the $[0001]_\alpha$ direction of the Mg matrix. The corresponding selected area electron diffraction (SAED) patterns are also inset.

The matrix precipitation of the peak-aged 0Y alloy is exhibited in Figs. 7(a) and (b). Three types of precipitates are found in the peak-aged 0Y alloy according to their typical features. The larger-scale $\{10\bar{1}0\}_\alpha$ plates (elongated along $\langle 11\bar{2}0\rangle_\alpha$ directions) are considered to be β_1 phases, which are reported to have the fcc structure [20−22]. The lenticular $\{11\bar{2}0\}_\alpha$ platelets (elongated along $\langle 10\bar{1}0\rangle_\alpha$ directions) are β''. As detailed in Fig. 8(a), in addition to β'' and β_1, some precipitates consisting of zigzag Nd-rich atomic columns are distributed unevenly in the vicinity of β_1 and β'' phases. These zigzag precipitates are ordered G.P. zones.

As shown in Figs. 7(c) and (d), the peak-aged 1.5Y alloy is mainly characterized by a dense distribution of lenticular $\{11\bar{2}0\}_\alpha$ precipitates. These lenticular $\{11\bar{2}0\}_\alpha$ precipitates are β'', which are consistent with those observed in the peak-aged 0Y alloy. The corresponding inset SAED pattern reveals the existence of extra diffraction spots at 1/2 $(10\bar{1}0)_\alpha$ positions, indicating the orientation relationship (OR) of $[0001]_{\beta''}//[0001]_\alpha$, and $(10\bar{1}0)_{\beta''}//(10\bar{1}0)_{Mg}$ between β'' phase and Mg. In addition, a small number of G.P. zones can still be observed in areas near some β''.

As indicated in Figs. 7(e) and (f), the key strengthening precipitates in the peak-aged 3.0Y alloy are $\{11\bar{2}0\}_\alpha$ β'' precipitates. The additional diffraction intensity illustrated by the corresponding inset SAED pattern (in Fig. 7(e)) is similar to that of the peak-aged 1.5Y alloy. In addition to lenticular β'', some globular precipitates connected by several β'' are visible. As detailed in Fig. 8(b), the globular precipitates can be characterized to be β' by the arrangements of single zigzag lines perpendicular to $\langle 11\bar{2}0\rangle_\alpha$ direction [23,24].

As exhibited in Figs. 7(g) and (h), it is noticeable that the number density of β' in the peak-aged 4.5Y alloy is significantly increased when compared with that in the peak-aged 3.0Y alloy, which is also confirmed by the specific sets of diffraction reflections at 1/4 $(01\bar{1}0)_\alpha$, 1/2 $(01\bar{1}0)_\alpha$ and 3/4 $(01\bar{1}0)_\alpha$ positions in the corresponding SAED pattern (Fig. 7(g)).

3.3.2 Peak-aged microstructure at 225 °C

Figure 9 presents the HAADF-STEM images illustrating the precipitate microstructure of alloys peak-aged at 225 °C in $[0001]_\alpha$ direction. Compared with the studied peak-aged alloys at 200 °C (illustrated in Fig. 7), the dominant strengthening precipitates for the studied alloys aged at 225 °C are similar to those aged at 200 °C. However, the number density of these dominant strengthening precipitates in the four alloys undergoes a visible reduction. Moreover, the dimensions of these precipitates are increased as the ageing temperature increases from 200 to 225 °C.

3.4 Mechanical properties of as-quenched and peak-aged alloys

The mechanical properties of as-quenched alloys are presented in Fig. 10. As the Y content increases from 0 to 4.5 wt.%, the ultimate tensile strength (UTS) and yield strength (YS) of the as-quenched 0Y alloy increase successively, from 195 and 109 MPa to 243 and 150 MPa, respectively.

Figures 11(a, b) show the typical tensile stress−strain curves of alloys peak-aged at 200 and 225 °C. The values of YS, UTS and elongation (EL) as a

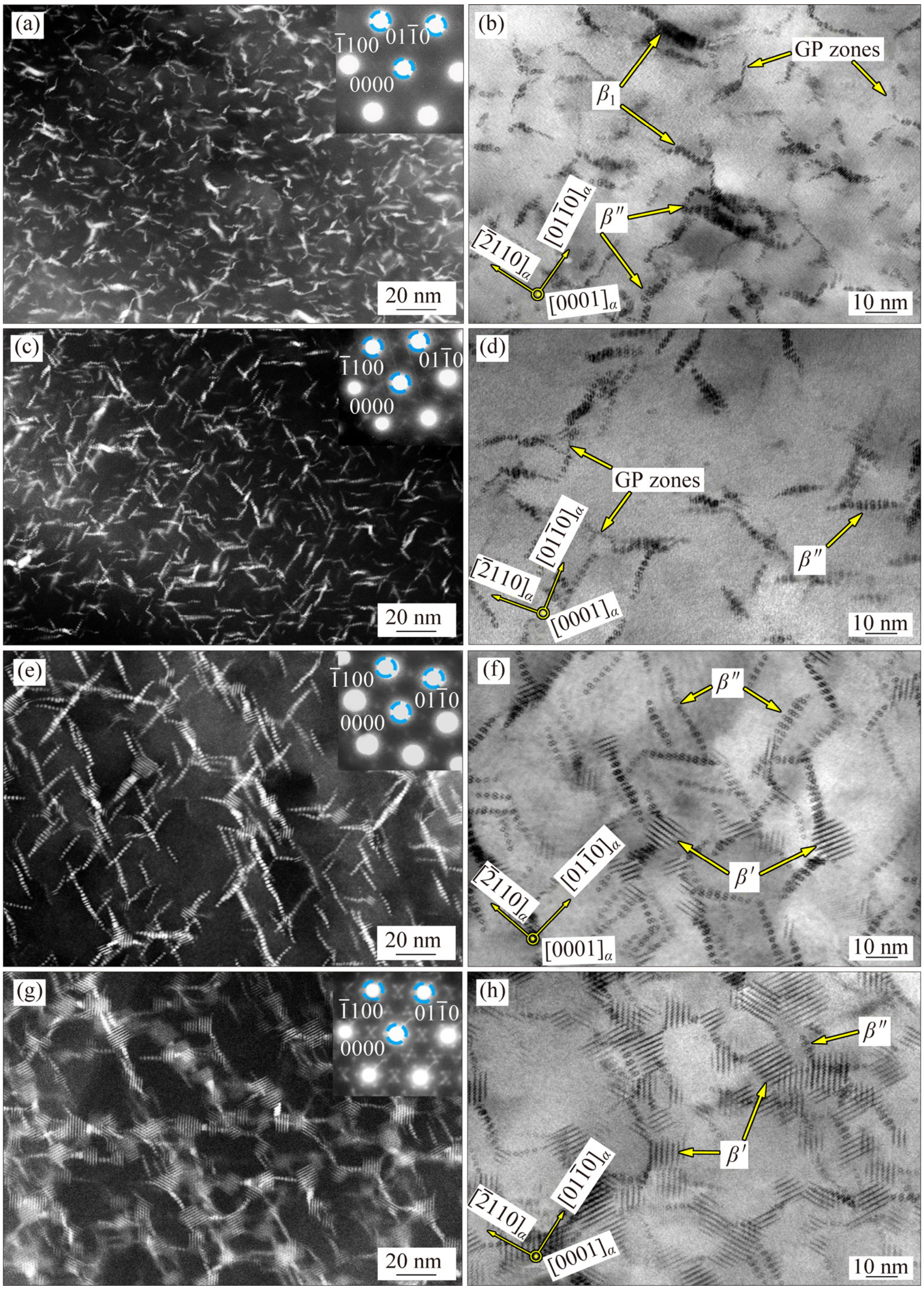

Fig. 7 Precipitation microstructures in alloys peak-aged at 200 °C: (a, b) 0Y alloy; (c, d) 1.5Y alloy; (e, f) 3.0Y alloy; (g, h) 4.5Y alloy (The micrographs in (a, c, e, g) are HAADF-STEM images with lower magnification, and the images in (b, d, f, h) are BF-STEM images with higher magnification. The incident beam is parallel to $[0001]_\alpha$ direction)

function of Y content are exhibited in Figs. 11(c−e), respectively. As illustrated in Fig. 11(c), the yield strength of peak-aged alloys is continually improved with the increasing Y content. The maximum YS increments are both achieved in the 4.5Y alloy during ageing at 200 and 225 °C, with the YS strongly increasing from 151 to 239 MPa (when isothermally aged at 200 °C) and increasing from 149 to 210 MPa (when isothermally aged at 225 °C).

Figure 11(d) provides the variation of the UTS of peak-aged alloys with different Y additions. As the Y content increases, continuous increments of UTS are observed in the peak-aged alloys aged at both 200 and 225 °C. Compared with the peak-aged 0Y alloy at 200 and 225 °C, the UTS observed in the 4.5Y alloy is enhanced by 39 MPa and 46 MPa, respectively.

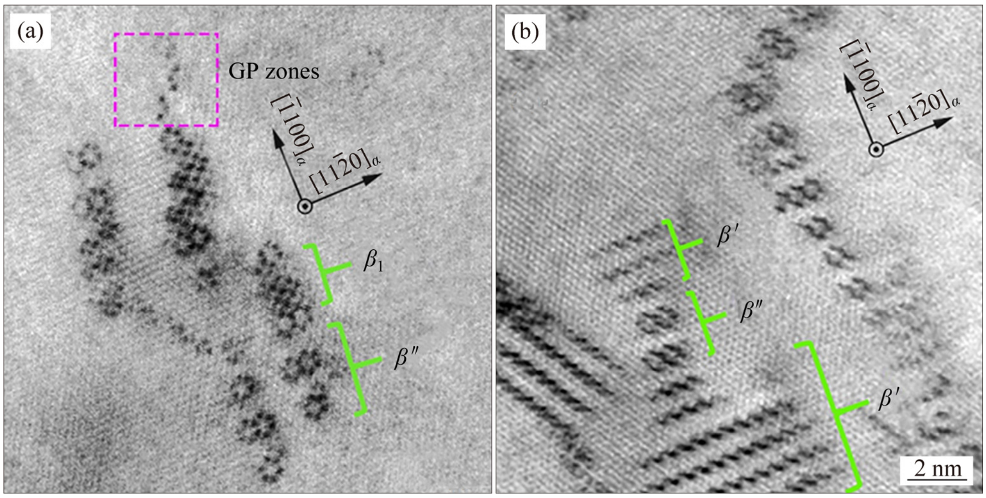

Fig. 8 BF-STEM image illustrating details of G.P. zones, β'' and β_1 precipitates observed in peak-aged 0Y alloy at 200 °C (a) and β'' and β' observed in peak-aged 3.0Y alloy at 200 °C (b) (The images are taken along $[0001]_\alpha$ direction)

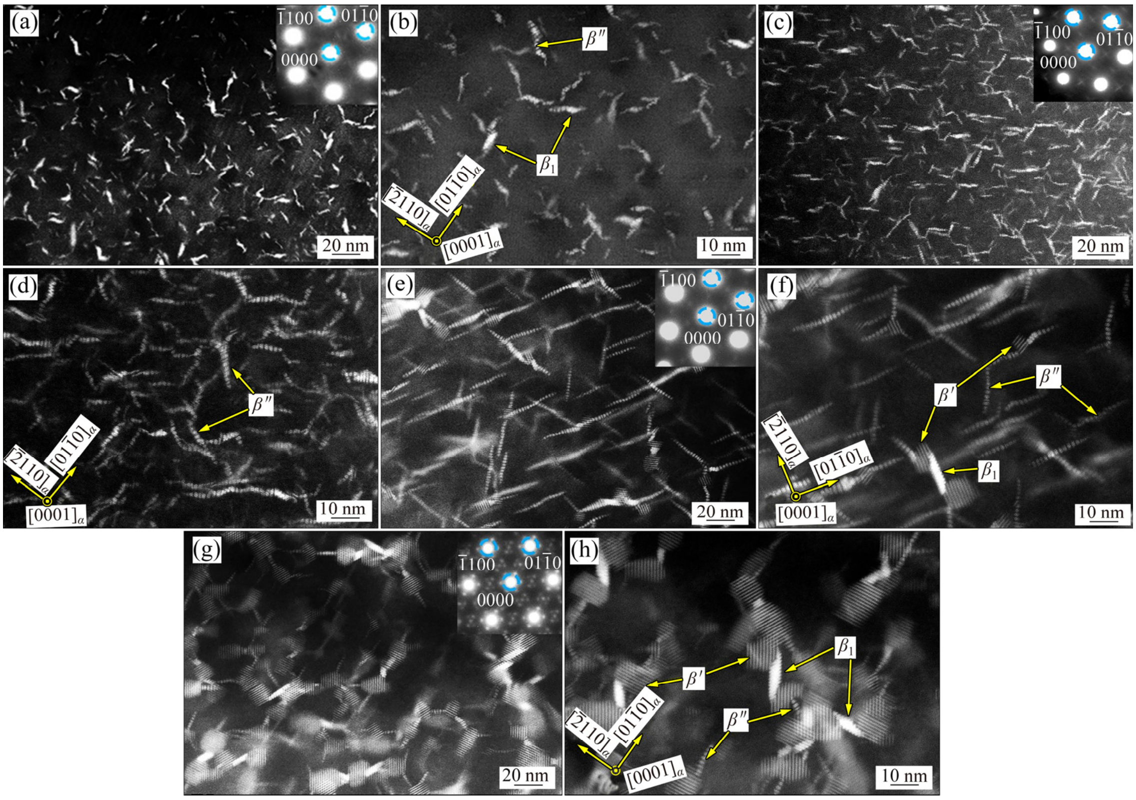

Fig. 9 HAADF-STEM images showing matrix precipitates in alloys peak-aged at 225 °C in $[0001]_\alpha$ direction: (a, b) 0Y alloy; (c, d) 1.5Y alloy; (e, f) 3.0Y alloy; (g, h) 4.5Y alloy

Figure 11(e) illustrates the change in elongation with various Y contents. The EL is found to be gradually decreased from 8.1% to 1.1% in peak-aged alloys when isothermally aged at 200 °C. Moreover, when isothermally aged at 225 °C, the EL of peak-aged-alloys experiences a trend of first increasing and then decreasing.

Table 3 lists the mechanical properties of the cast Mg−Y−Nd system alloys reported by the previous and present work. The ultimate tensile strength (UTS) of the peak-aged 3.0Y and 4.5Y alloys under different ageing conditions are higher than 300 MPa. The peak-aged studied 3.0Y and 4.5Y alloys exhibit comparable or even better mechanical properties than the traditional Mg−Y−Nd system alloys.

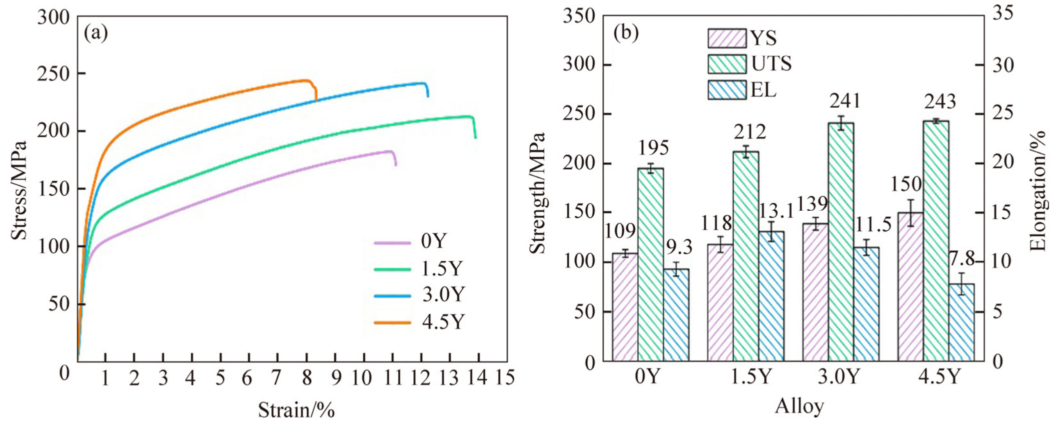

Fig. 10 Tensile stress−strain curves (a) and mechanical properties (b) of as-quenched alloys

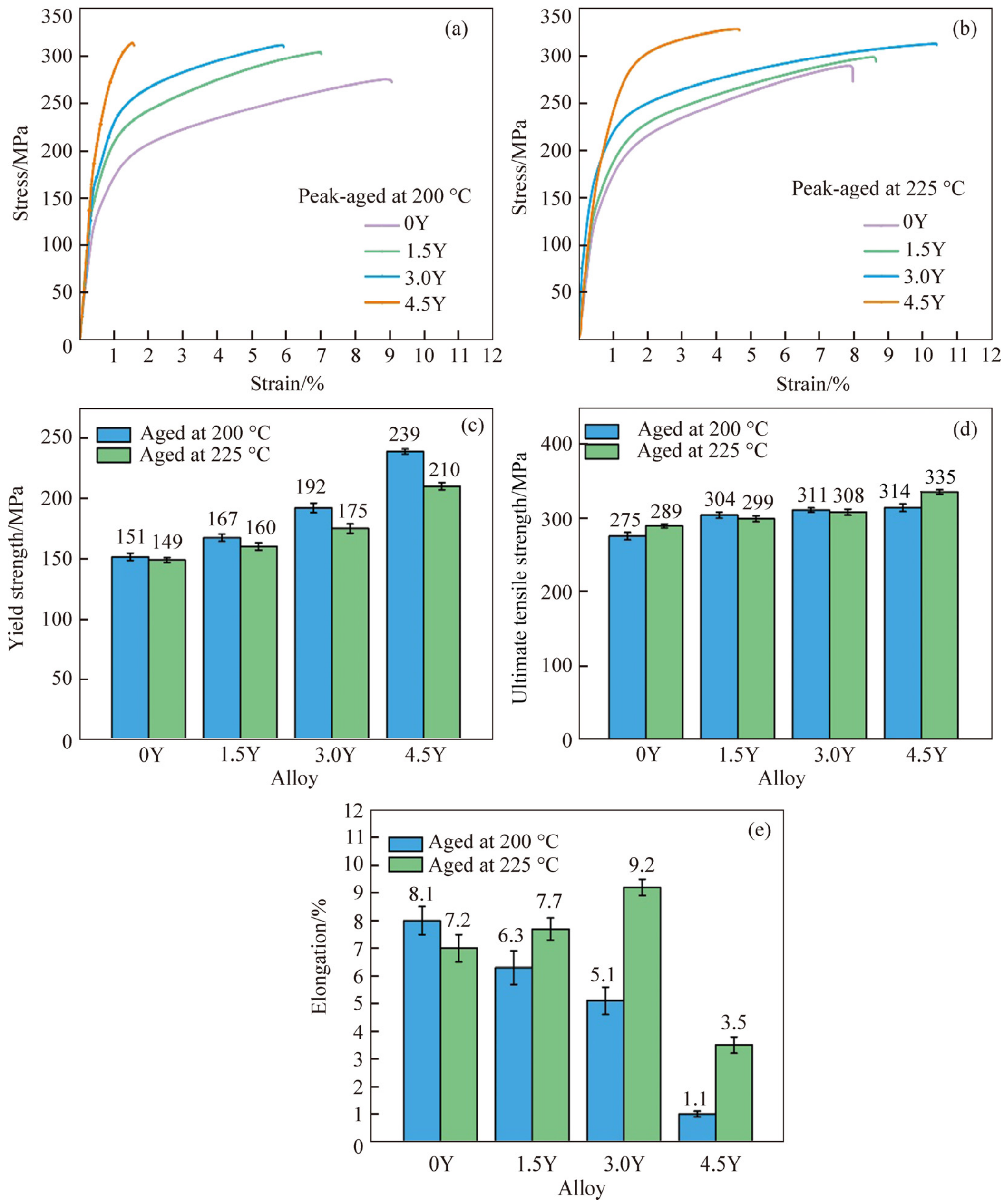

Fig. 11 Tensile stress−strain curves of alloys peak-aged at 200 °C (a) and 225 °C (b), yield strength (c), ultimate tensile strength (d) and elongation (e) of peak-aged alloys as function of Y content

4 Discussion

4.1 Promoted precipitation of β' associated with Y additions

As described above, it is noted that the age-hardening response of the 0Y alloy is significantly enhanced with the increasing Y content. According to the corresponding peak-aged microstructure, in the peak-aged Y-free alloy, β'' and β_1 are the main strengthening precipitates, which is consistent with the Mg−Nd binary alloys [24]. However, with the additions of Y, β' can be found in the peak-aged Y-containing alloys, and their number density progressively increases as Y content increases. The promoted precipitation of β' due to Y additions substantially improves the age-hardening response.

For binary Mg−RE alloys, ageing treatment leads to the formation of G.P. zones, followed by one or more metastable precipitates involving β'', β' and β_1 [24,31,32]. In binary Mg−Y alloys, only β' is found [24,33]. For binary Mg−Nd alloys, the precipitation sequence has been reported to involve β'', β' and β_1 [21,34]. When Y is added to Mg−Nd alloys, precipitate evolution in the binary Mg−Y system (β') and Mg−Nd system (β'', β', β_1) might concurrently progress in Mg−Y−Nd alloys. This speculation can be supported by the element distribution in the dominant strengthening precipitates of the 4.5Y alloy involving β'', β' and β_1 (revealed in Figs. 12 and 13). As shown in Fig. 12, Y is mainly enriched in β', and Nd element is enriched in both β' and β''. As illustrated in Fig. 13, enrichment of Y in β' is also observed. Meanwhile, in addition to the strong segregation in β', Nd is also significantly enriched in β_1. The elemental mapping results reveal that Y is mainly enriched in β' while Nd is enriched in β'', β' and β_1, suggesting that Y is mainly involved in the formation of β' while Nd is involved in the formation of β'', β' and β_1.

4.2 Influence of ageing temperature on matrix precipitation

Table 4 provides the size and distribution of the key strengthening precipitates of the peak-aged alloys at 200 and 225 °C. The increased ageing temperature might affect the precipitation in two aspects: by decreasing the number density of precipitates and subsequently increasing the size of the precipitate.

On the one hand, as the ageing temperature increases, the number density of precipitates is expected to successively decrease as the driving force for precipitation (i.e. the volume free energy difference of the alloy system) decreases with increasing the ageing temperature from 200 to 225 °C [35]. On the other hand, the size of precipitates is mainly controlled by the critical nucleation radius and the coarsening rate. With the increase of the ageing temperature, the critical nucleation radius of the precipitates also increases

Table 3 Mechanical properties of typical cast Mg−Y−Nd alloys in T6 state (Data from present work and literature)

Alloy	Condition	YS/MPa	UTS/MPa	EL/%	Ref.
Mg−3Nd−3Y−0.2Zn−0.5Zr	T6(200 °C)	192±4	311±3	5.1±0.5	This work
	T6(225 °C)	175±4	308±4	9.2±0.3	
Mg−3Nd−4.5Y−0.2Zn−0.5Zr	T6(200 °C)	239±2	314±5	1.1±0.1	This work
	T6(225 °C)	210±3	335±2	3.5±0.3	
Mg−5Y−2.5Nd−1.5Gd−0.5Zr	T6	195±11	284±8	9.7±1.0	[25]
Mg−4Y−2.4Nd−0.2Zn−0.4Zr	T6	195	260	3.0	[26]
Mg−4Y−2.3Nd−1.0Gd−0.4Zr	T6	193	260	3.0	[27]
Mg−4Y−3Nd−1Gd−0.2Zn−0.5Zr	T6	198	276	7.6	[28]
Mg−4Y−2.3Nd−1Gd−0.6Zr	T6	202±1.5	282±10.1	1.0±0.9	[28]
Mg−4Y−2.5Nd−0.7Zr	T6	175	293	5.6	[29]
WE54	T6	208	261	2.3	[30]
WE43	T6	196	345	7.3	[30]

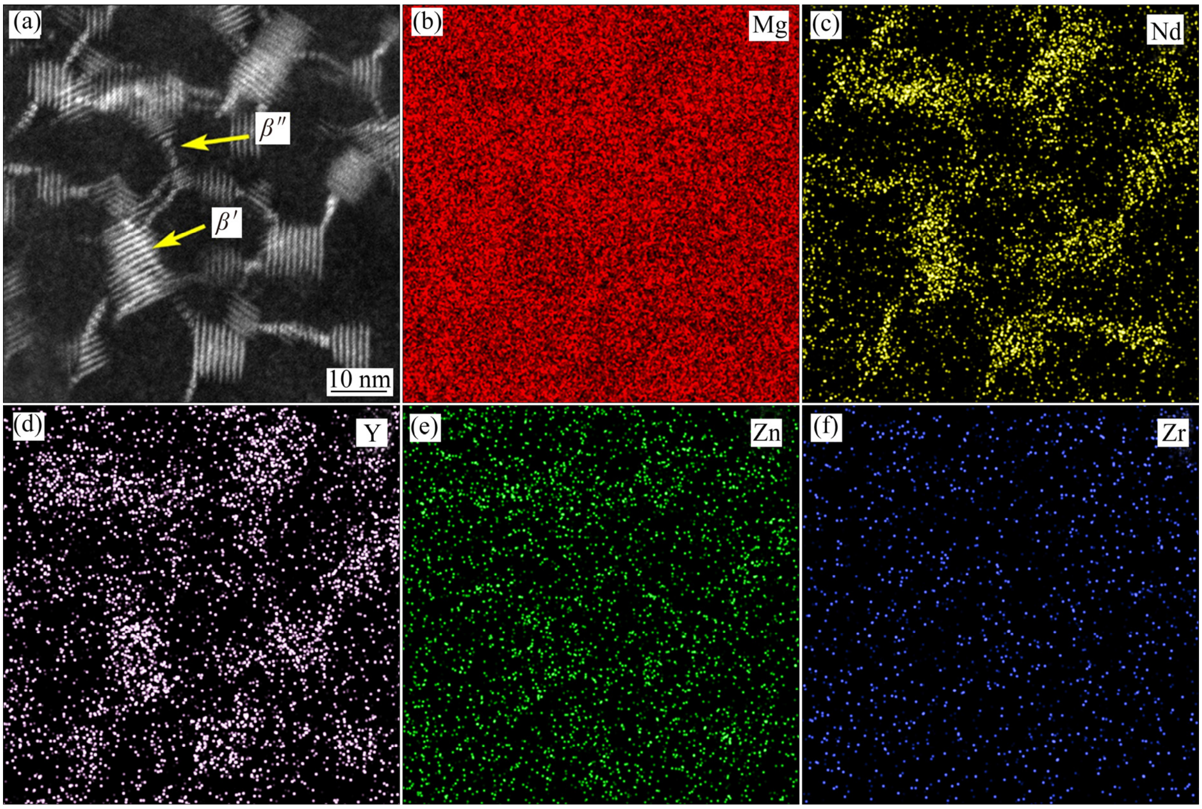

Fig. 12 HAADF-STEM image obtained from peak-aged 4.5Y alloy (aged at 200 °C for 128 h) viewed in $[0001]_\alpha$ direction (a) and corresponding EDS elemental maps of Mg (b), Nd (c), Y (d), Zn (e) and Zr (f)

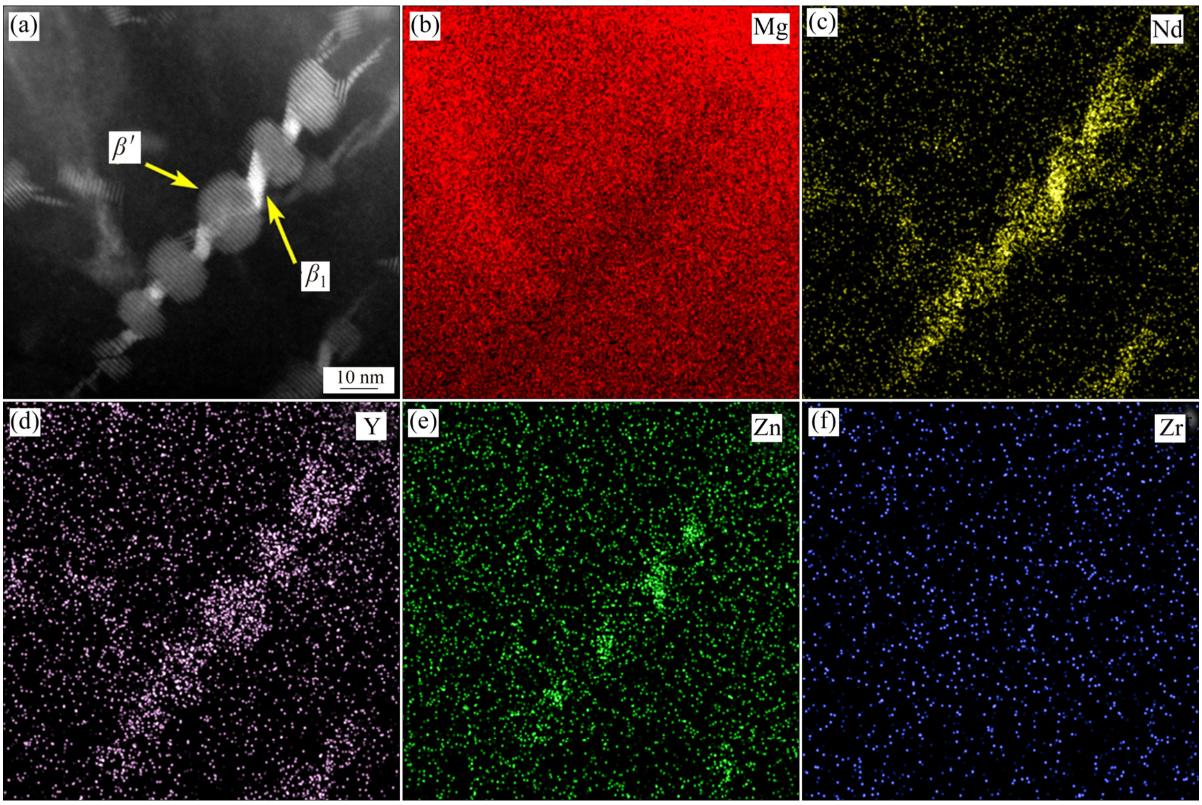

Fig. 13 HAADF-STEM image obtained from peak-aged 4.5Y alloy (aged at 225 °C for 16 h) viewed in $[0001]_\alpha$ direction (a) and corresponding EDS elemental maps of Mg (b), Nd (c), Y (d), Zn (e) and Zr (f)

Table 4 Quantitative measurements of precipitates in peak-aged alloys

Alloy	Precipitate	Peak-aged state at 200 °C			Peak-aged state at 225 °C		
		Length/nm	Width/nm	Area number density/ $10^{15}m^{-2}$	Length/nm	Width/nm	Area number density/$10^{15}m^{-2}$
0Y	G.P. zones	−	−	0.9	−	−	Ignored
	β''	7.9	1.8	6.5	10.5	2.2	5.9
	β_1	6.5	1.8	0.7	8.2	2.6	0.9
1.5Y	G.P. zones	−	−	0.7	−	−	Ignored
	β''	10.8	1.9	8.5	12.5	2.1	7.9
	β_1	−	−	Ignored	−	−	Ignored
3.0Y	β''	15.8	2.0	7.8	20.9	2.0	5.9
	β'	7.6	7.9	3.0	11.2	10.1	2.8
	β_1	−	−	Ignored	12.1	3.8	0.4
4.5Y	β''	6.3	1.9	5.1	10.0	2.0	3.4
	β'	8.5	8.1	7.9	13.4	10.9	5.6
	β_1	−	−	Ignored	13.2	4.1	0.8

The thickness and length of β'' and β' are measured along $\langle 11\bar{2}0\rangle_\alpha$ and $\langle 10\bar{1}0\rangle_\alpha$ directions, respectively, in $[0001]_\alpha$ projected images. The thickness and length of β_1 are measured along $\langle 10\bar{1}0\rangle_\alpha$ and $\langle 11\bar{2}0\rangle_\alpha$ directions, respectively, in $[0001]_\alpha$ projected images

with the decreased driving force for precipitation according to the classical nucleation theory [36,37]. For determining the coarsening rate, we used the Lifshitz−Slyozov−Wagner (LSW) kinetic equations developed for precipitate coarsening [38]:

$$\bar{R}^3 - R_{co}^3 = Kt \tag{1}$$

$$K = \frac{8\sigma D C_e V_m}{9RT} \tag{2}$$

where $\bar{R}$ is the mean measured particle size, R_{co} the initial critical size for the growth, K the coarsening rate constant, D the diffusion coefficient of solute in the matrix, C_e the equilibrium solute concentration of the matrix at the ageing temperature T, σ the interfacial free energy, V_m the molar volume of the precipitate, and R the molar gas constant.

D and T are two significant factors influencing the precipitate coarsening rate. Table 5 lists the calculated diffusion coefficient D of Nd and Y in Mg matrix at 200 and 225 °C. Increasing the temperature from 200 (473 K) to 225 °C (498 K) can enhance the diffusion coefficients of Y and Nd elements by approximately four and five times, respectively. The increased ageing temperature substantially improves the diffusion coefficient of Nd or Y, leading to an obvious acceleration of the coarsening process.

Table 5 Diffusion coefficients (D) of Nd and Y in Mg matrix at 200 and 225 °C

Element	D in Mg [39]	D at 200 °C/ ($m^2 \cdot s^{-1}$)	D at 225 °C/ ($m^2 \cdot s^{-1}$)
Y	$8.4\times10^{-6}\cdot \exp[-126987/(RT)]$	7.94×10^{-20}	4.02×10^{-19}
Nd	$1.3\times10^{-6}\cdot \exp[-111230/(RT)]$	6.76×10^{-19}	2.79×10^{-18}

4.3 Enhanced yield strength associated with Y additions

As mentioned above, Y additions gradually improve the yield strength of the as-quenched and peak-aged Mg−3Nd−0.2Zn−0.5Zr alloys. The primary strengthening mechanisms under the as-quenched and peak-aged conditions are analyzed as follows to better clarify the influence of Y additions on the yield strength.

4.3.1 Main strengthening mechanisms of as-quenched alloys

As for as-quenched alloys, the dominant strengthening mechanisms are the grain boundary strengthening and solid-solution strengthening [17]. Y additions mainly enhance the strength of the as-quenched 0Y alloy by affecting these two factors. On the one hand, the Hall–Petch equation describes the contribution of grain size to the YS (σ) as follows [40,41]:

$$\sigma=\sigma_0+k\overline{d}^{-1/2} \quad (3)$$

where σ_0 is the friction stress, k the Hall–Petch coefficient, and $\overline{d}$ the average grain size.

As illustrated in Fig. 4, the $\overline{d}$ values of the as-quenched 0Y, 1.5Y, 3Y and 4.5Y alloys are 35, 27, 24 and 29 μm, respectively. By referring to the reported Hall–Petch coefficient of the as-quenched Mg−3Nd−0.2Zn alloy (9.1 MPa·mm$^{1/2}$) [40], the improvements of YS ($\Delta\sigma_{gb}$) by the grain refinements caused by 1.5, 3.0 and 4.5 wt.% Y additions can be estimated to be approximately 6.7, 10.1 and 4.7 MPa, respectively.

On the other hand, the solid solution strengthening effects (σ_{ss}) can be described by the following equation [10,17,42]:

$$\sigma_{ss}=Cx^{2/3} \quad (4)$$

where C is a constant referring to the strengthening rate, and x is the molar fractions of solute atoms.

Since C_Y is reported to be 800 MPa at.$^{-2/3}$ [42], the maximum solid solution strengthening effects ($\Delta\sigma_{ss}$) associated with 1.5, 3.0 and 4.5 wt.% Y additions can be calculated to be 15.9, 31.8 and 47.7 MPa, respectively. According to the tensile test results of the as-quenched samples (provided in Fig. 10), the increments in yield strength of as-quenched alloys ($\Delta\sigma_{\text{as-quenched}}=\sigma_{\text{as-quenched Y-containing alloy}}-\sigma_{\text{as-quenched 0Y alloy}}$) associated with 1.5, 3 and 4.5 wt.% Y are 9, 30 and 41 MPa, respectively. Thus, the actual solid solution strengthening effect ($\Delta\sigma_{ss}=\Delta\sigma_{\text{as-quenched}}-\Delta\sigma_{gb}$) associated with Y additions can be estimated to be 2.3, 19.9 and 36.3 MPa, respectively. As illustrated in Table 6, it is noted that the actual solid solution strengthening effects ($\Delta\sigma_{ss}$) are less than the maximum solid solution strengthening effects ($\Delta\sigma_{ssmax}$) with different Y additions, which is mainly attributed to the existence of residual secondary phases. The existence of residual secondary phases will inevitably consume solute Y atoms. Thus, the solid solution strengthening effect of Y is lower than the maximum value obtained by theoretical calculation.

4.3.2 Main strengthening mechanisms of peak-aged alloys

In peak-aged alloys, the solid solution strengthening contribution is remarkably decreased due to the depletion of solutes associated with the precipitation process [43,44]. The increase in YS of the alloys related to Y additions is largely due to the changed precipitate microstructure. According to the measured number density of precipitates shown in Table 4, the main strengthening precipitate in peak-aged 0Y and 1.5Y alloys is β'' while those in peak-aged 3.0Y and 4.5Y alloys are β'' and β' precipitates. Compared with the peak-aged 0Y alloy, the area number density of β'' increases from 6.5×10^{15} and 5.9×10^{15}/m^2 to 8.5×10^{15} and 7.9×10^{15}/m^2, respectively, when peak-aged at 200 and 225 °C. Thus, it can be inferred that this increment of YS associated with 1.5 wt.% Y addition is mainly ascribed to the increasing volume fraction of β''. Additionally, as Y content is increased from 1.5 wt.% to 4.5 wt.%, the area number density of β'' gradually decreases from 8.5×10^{15} and 7.9×10^{15}/m^2 to 5.1×10^{15} and 3.4×10^{15}/m^2, respectively, when the specimen is peak-aged at 200 and 225 °C. However, it is noteworthy the area number density of extra β' is significantly improved to 7.9×10^{15} and 5.6×10^{15}/m^2 when the specimen is peak-aged at 200 and 225 °C, respectively. Thus, it is suggested that significant increment in YS due to a further increase in Y content is mainly attributed to the noticeable increase in the volume fraction of β' precipitates.

Table 6 Strengthening contributions associated with Y additions under as-quenched condition

Strengthening contributions	1.5Y	3.0Y	4.5Y
Increment of yield strength, $\Delta\sigma_{\text{as-quenched}}$/MPa	9	30	41
Increment of grain boundaries strengthening, $\Delta\sigma_{gb}$/MPa	6.7	10.1	4.7
Increment of actual solid solution strengthening, $\Delta\sigma_{ss}$/MPa	2.3	19.9	36.3
Increment of calculated maximum solid solution strengthening, $\Delta\sigma_{ssmax}$/MPa	15.9	31.8	47.7

4.4 Role of Y addition and ageing temperature on ductility of alloys

As indicated by Figs. 10 and 11, it is noted that the Y addition exerts pronounced influences on the elongation of as-quenched and peak-aged alloys. For the as-quenched samples, the elongation of studied alloys first increases and then decreases with increasing Y content. As reported previously, the solid solution of Y atoms in the Mg matrix can promote the activation of the non-basal slip system [45]. Thus, it is reasonable that increasing Y content should enhance the ductility of the as-quenched alloy. However, as shown in Figs. 4 and 5, as Y content increases, residual secondary phases inevitably appear near the grain boundaries, the presence of which is detrimental to the alloy ductility [46]. After the ageing treatment, Y additions mainly influence the ductility of peak-aged alloys by changing the precipitate microstructure. These precipitates are able to hinder the movement of dislocations, thereby significantly affecting the plasticity of the alloys [47,48]. Since the size, type and quantity of key strengthening precipitates in the peak-aged alloys are concurrently varied with the increase of Y content, it is difficult to analyze the influence of different precipitates on the plasticity quantitatively. However, compared the 4.5Y with the 0Y alloy, it is noticeable that the plasticity of the alloy will decrease significantly when the volume fraction of the β' precipitates increases obviously. Moreover, as indicated in Section 4.2, increasing the ageing temperature significantly reduces the number density of the dominant precipitates. That is why the elongation of peak-aged alloys presents an upwards trend with the increasing ageing temperature.

5 Conclusions

(1) As the Y content increases, the dominant secondary phases in as-cast alloys are found to change from $Mg_{12}Nd$ to $Mg_{24}Y_5$-type phases.

(2) The number density of Zn−Zr particles in the grains of the as-quenched alloys decreases gradually with the increasing Y content.

(3) Y is found to be highly enriched in β'. The addition of Y promotes the precipitation of prismatic β'.

(4) The increments of YS associated with 4.5 wt.% Y addition are 88 and 61 MPa, in the 200 and 225 °C peak-aged conditions, respectively, which is mainly attributed to the uniform and dense distribution of β'.

(5) Increasing the ageing temperature can enhance the size but decrease the number density of key strengthening precipitates in peak-aged Mg−xY−3Nd−0.2Zn−0.5Zr alloys.

(6) Mg−3Y−3Nd−0.2Zn−0.5Zr alloy exhibits better combination of strength and ductility (200 °C ageing: YS=192 MPa, UTS=311 MPa, EL=5.1%; 225 °C ageing: YS=175 MPa, UTS=308 MPa, EL=9.2%).

Acknowledgments

This research was supported by the National Natural Science Foundation of China (Nos. U2037601, 51775334 and 51821001), the National Key Research & Development Program of China (No. 2016YFB0701205), the Joint Innovation Fund of CALT and College, China (No. CALT2020-TS07), the Open Fund of State Key Laboratory of Advanced Forming Technology and Equipment, China (No. SKL2020005), and the Research Program of Joint Research Center of Advanced Spaceflight Technologies, China (No. USCAST2020-14).

References

[1] WU Guo-hua, WANG Cun-long, SUN Ming, DING Wen-jiang. Recent developments and applications on high-performance cast magnesium rare-earth alloys [J]. Journal of Magnesium and Alloys, 2021, 9(1): 1−20.

[2] LIU Wei, DU Zhi-wei, LI Ting, ZHANG Kui, HAN Xiao-lei, PENG Yong-gang, ZHANG Jing, YUAN Jia-wei, LIU Shu-feng, PANG Zheng. Precipitate evolution in Mg−7Gd−3Y−1Nd−1Zn−0.5Zr alloy during isothermal ageing at 240 °C [J]. Transactions of Nonferrous Metals Society of China, 2019, 29(10): 2047−2055.

[3] WU Luo-yi, LI Hao-tian, YANG Zhong. Microstructure evolution during heat treatment of Mg–Gd–Y–Zn–Zr alloy and its low-cycle fatigue behavior at 573 K [J]. Transactions of Nonferrous Metals Society of China, 2017, 27(5): 1026−1035.

[4] LIU Hong-hui, NING Zhi-liang, YI Jun-ying, MA Qian, SUN Hai-chao, HUANG Yong-jiang, SUN Jian-fei. Effect of Dy addition on microstructure and mechanical properties of Mg−4Y−3Nd−0.4Zr alloy [J]. Transactions of Nonferrous Metals Society of China, 2017, 27(4): 797−803.

[5] LIU Zhi-jie, WU Guo-hua, LIU Wen-cai, PANG Song, DING Wen-jiang. Effect of heat treatment on microstructures and mechanical properties of sand-cast Mg−4Y−2Nd–1Gd–0.4Zr magnesium alloy [J]. Transactions of Nonferrous Metals Society of China, 2012, 22(7): 1540−1548.

[6] TIAN Zheng, YANG Qiang, GUAN Kai, CAO Zhan-Yi, MENG Jian. Microstructural evolution and aging behavior of Mg–4.5Y–2.5Nd–1.0Gd–0.5Zr alloys with different Zn additions [J]. Rare Metals, 2021, 40(8): 2188−2196.

[7] GUO Yan-lin, LIU Bin, XIE Wei, LUO Qun, LI Qian. Anti-phase boundary energy of β series precipitates in Mg−Y−Nd system [J]. Scripta Materialia, 2021, 193: 127−131.

[8] PENG Yong-gang, DU Zhi-wei, LIU Wei, LI Yong-jun, LI Ting, HAN Xiao-lei, MA Ming-long, PANG Zheng, YUAN Jia-wei, SHI Guo-liang. Evolution of precipitates in

Mg−7Gd−3Y−1Nd−1Zn−0.5Zr alloy with fine plate-like 14H-LPSO structures aged at 240 °C [J]. Transactions of Nonferrous Metals Society of China, 2020, 30(6): 1500−1510.

[9] ZHOU Yi-yuan, FU Peng-huai, PENG Li-ming, WANG Dan, WANG Ying-xin, HU Bin, LIU Ming, SACHDEV A K, DING Wen-jiang. Precipitation modification in cast Mg–1Nd–1Ce–Zr alloy by Zn addition [J]. Journal of Magnesium and Alloys, 2019, 7(1): 113−123.

[10] SHENG L Y, DU B N, HU Z Y, QIAO Y X, XIAO Z P, WANG B J, XU D K, ZHENG Y F, XI T F. Effects of annealing treatment on microstructure and tensile behavior of the Mg−Zn−Y−Nd alloy [J]. Journal of Magnesium and Alloys, 2020, 8(3): 601−613.

[11] NIE J F, MUDDLE B C. Precipitation in magnesium alloy WE54 during isothermal ageing at 250 °C [J]. Scripta Materialia, 1999, 40(10): 1089−1094.

[12] NIE J F, MUDDLE B C. Characterisation of strengthening precipitate phases in a Mg–Y–Nd alloy [J]. Acta Materialia, 2000, 48: 1691−1703.

[13] PENG Chong-hao, LI De-jiang, ZENG Xiao-qin, DING Wen-jiang. First principles investigation of β'-short and β'-long in Mg–Gd alloy [J]. Journal of Alloys and Compounds, 2016, 671: 177−183.

[14] ROKHLIN L L. Magnesium alloys containing rare earth metals [M]. London: CRC Press, 2003.

[15] ZHAO Xin-yi, NING Zhi-liang, LI Zhong-quan, ZOU Wen-bing, LI Bao-hui, HE Kai, CAO Fu-yang, SUN Jian-fei, LUO A A. In-mold oxidation behavior of Mg–4.32Y–2.83Nd–0.41Zr alloy [J]. Journal of Materials Science, 2018, 53(15): 11091−11103.

[16] LUO Kang, ZHANG Liang, WU Guo-hua, LIU Wen-cai, DING Wen-jiang. Effect of Y and Gd content on the microstructure and mechanical properties of Mg–Y–RE alloys [J]. Journal of Magnesium and Alloys, 2019, 7(2): 345−354.

[17] XIE He, WU Guo-hua, ZHANG Xiao-long, LIU Wen-cai, DING Wen-jiang. The role of Gd on the microstructural evolution and mechanical properties of Mg−3Nd−0.2Zn−0.5Zr alloy [J]. Materials Characterization, 2021, 175: 111076.

[18] ZENGIN H, TUREN Y. Effect of Y addition on microstructure and corrosion behavior of extruded Mg−Zn−Nd−Zr alloy [J]. Journal of Magnesium and Alloys, 2020, 8(3): 640−653.

[19] XIE He, WU Guo-hua, ZHANG Xiao-long, ZHANG Jin-shuo, DING Wen-jiang. The role of Yb content on the microstructural evolution and mechanical characteristics of cast Mg−9Gd−0.5Zn−0.2Zr alloy [J]. Materials Science and Engineering: A, 2021, 817: 141292.

[20] XIA Xiang-yu, SANATY-ZADEH A, ZHANG Chuan, LUO A A, STONE D S. Experimental investigation and simulation of precipitation evolution in Mg−3Nd−0.2Zn alloy [J]. Calphad, 2018, 60: 58−67.

[21] TAN J, DONG Y, ZHANG H X, SUN Y H, SUN B Z, QI Y. A new insight into the beta‴ structure: Three categories of configurations between beta′ precipitates in aged binary Mg−Nd alloy [J]. Scripta Materialia, 2019, 172: 130−134.

[22] GUI Zhen-zhen, WANG Fen, ZHANG Jun-yi, CHEN De-xin, KANG Zhi-xin. Precipitation behaviors and mechanical properties of a solution-treated Mg−Gd−Nd−Zn−Zr alloy during equal-channel angular pressing process [J]. Journal of Magnesium and Alloys, 2022, 10(1): 239−248.

[23] HE S M, ZENG X Q, PENG L M, GAO X, NIE J F, DING W J. Precipitation in a Mg–10Gd–3Y–0.4Zr (wt.%) alloy during isothermal ageing at 250 °C [J]. Journal of Alloys and Compounds, 2006, 421(1/2): 309−313.

[24] NIE Jian-feng. Precipitation and hardening in magnesium alloys [J]. Metallurgical and Materials Transactions A, 2012, 43(11): 3891−3939.

[25] TIAN Zheng, YANG Qiang, GUAN Kai, MENG Jian, CAO Zhan-yi. Microstructure and mechanical properties of a peak-aged Mg−5Y−2.5Nd−1.5Gd−0.5Zr casting alloy [J]. Journal of Alloys and Compounds, 2018, 731: 704−713.

[26] SU Zai-jun, LIU Chu-ming, WAN Ying-chun. Microstructures and mechanical properties of high performance Mg−4Y−2.4Nd−0.2Zn−0.4Zr alloy [J]. Materials & Design, 2013, 45: 466−472.

[27] KANG Yue-hua, YAN Hong, CHEN Rong-shi. Effects of heat treatment on the precipitates and mechanical properties of sand-cast Mg–4Y–2.3Nd–1Gd–0.6Zr magnesium alloy [J]. Materials Science and Engineering: A, 2015, 645: 361−368.

[28] ZHANG Hao-hao, FAN Jian-feng, ZHANG Liang, WU Guo-hua, LIU Wen-cai, CUI Wen-dong, FENG Shi. Effect of heat treatment on microstructure, mechanical properties and fracture behaviors of sand-cast Mg−4Y−3Nd−1Gd−0.2Zn−0.5Zr alloy [J]. Materials Science and Engineering: A, 2016, 677: 411−420.

[29] XU Lu, LIU Chu-ming, WAN Ying-chun, WANG Xiao, XIAO Hong-chao. Effects of heat treatments on microstructures and mechanical properties of Mg−4Y−2.5Nd−0.7Zr alloy [J]. Materials Science and Engineering: A, 2012, 558: 1−6.

[30] WANG Dan, FU Peng-huai, PENG Li-ming, WANG Ying-xin, DING Wen-jiang. Development of high strength sand cast Mg–Gd–Zn alloy by co-precipitation of the prismatic β' and β_1 phases [J]. Materials Characterization, 2019, 153: 157−168.

[31] SOLOMON E L S, ARAULLO-PETERS V, ALLISON J E, MARQUIS E A. Early precipitate morphologies in Mg−Nd−(Zr) alloys [J]. Scripta Materialia, 2017, 128: 14−17.

[32] SHI Zhang-zhi, CHEN Hong-ting, ZHANG Ke, DAI Fu-zhi, LIU Xue-feng. Crystallography of precipitates in Mg alloys [J]. Journal of Magnesium and Alloys, 2021, 9(2): 416−431.

[33] SOLOMON E L S, NATARAJAN A R, ROY A M, SUNDARARAGHAVAN V, van der VEN A, MARQUIS E A. Stability and strain-driven evolution of β' precipitate in Mg−Y alloys [J]. Acta Materialia, 2019, 166: 148−157.

[34] SUN B Z, TAN J, ZHANG H X, SUN Y H. Atomic scale investigation of a novel metastable structure in aged Mg−Nd alloys [J]. Scripta Materialia, 2019, 161: 6−12.

[35] ZHANG Ke-long, LI Hui-zhong, LIANG Xiao-peng, CHEN Zhi, WANG Li. Discontinuous and continuous precipitation characteristics and mechanical properties of a AZ80A magnesium alloy at different aging temperatures [J]. Materials Characterization, 2020, 161: 110146.

[36] LIU F, SOMMER F, BOS C, MITTEMEIJER E J. Analysis of solid state phase transformation kinetics: Models and

recipes [J]. International Materials Reviews, 2007, 52(4): 193−212.

[37] CHRISTIAN J W. The theory of transformations in metals and alloys [M]. Oxford, UK: Pergamon Press.

[38] XU Pian, JIANG Feng, TANG Zhong-qin, YAN Ning, JIANG Jing-yu, XU Xu-da, PENG Yong-yi. Coarsening of Al_3Sc precipitates in Al−Mg−Sc alloys [J]. Journal of Alloys and Compounds, 2019, 781: 209−215.

[39] ZHOU Bi-cheng, SHANG Shun-li, WANG Yi, LIU Zi-kui. Diffusion coefficients of alloying elements in dilute Mg alloys: A comprehensive first-principles study [J]. Acta Materialia, 2016, 103: 573−586.

[40] LI Z M, LUO A A, WANG Q G, PENG L M, FU P H, WU G H. Effects of grain size and heat treatment on the tensile properties of Mg–3Nd–0.2Zn (wt%) magnesium alloys [J]. Materials Science and Engineering: A, 2013, 564: 450−460.

[41] NING Z L, LIU H H, CAO F Y, WANG S T, SUN J F, QIAN M. The effect of grain size on the tensile and creep properties of Mg−2.6Nd−0.35Zn−*x*Zr alloys at 250 °C [J]. Materials Science and Engineering: A, 2013, 560: 163−169.

[42] TODA-CARABALLO I, GALINDO-NAVA E I, RIVERA-DÍAZ-DEL-CASTILLO P E J. Understanding the factors influencing yield strength on Mg alloys [J]. Acta Materialia, 2014, 75: 287−296.

[43] HE S M, ZENG X Q, PENG L M, GAO X, NIE J F, DING W J. Microstructure and strengthening mechanism of high strength Mg–10Gd–2Y–0.5Zr alloy [J]. Journal of Alloys and Compounds, 2007, 427(1/2): 316−323.

[44] WANG Dan, FU Peng-huai, PENG Li-ming, WANG Ying-xin, DING Wen-jiang. A study of microstructure, mechanical behavior and strengthen mechanism in the Mg−10Gd−0.2Zn−(Y)−0.4Zr alloy [J]. Materials Science and Engineering: A, 2020, 793: 139881.

[45] SANDLÖBES S, FRIÁK M, ZAEFFERER S, DICK A, YI S, LETZIG D, PEI Z, ZHU L F, NEUGEBAUER J and RAABE D. The relation between ductility and stacking fault energies in Mg and Mg–Y alloys [J]. Acta Materialia, 2012, 60(6/7): 3011−3021.

[46] FU Peng-huai, PENG Li-ming, JIANG Hai-yan, CHANG Jian-wei, ZHAI Chun-quan. Effects of heat treatments on the microstructures and mechanical properties of Mg–3Nd–0.2Zn–0.4Zr (wt.%) alloy [J]. Materials Science and Engineering: A, 2008, 486(1/2): 183−192.

[47] SOLOMON E L S, MARQUIS E A. Deformation behavior of β' and β''' precipitates in Mg−RE alloys [J]. Materials Letters, 2018, 216: 67−69.

[48] HUANG Zhi-hua, YANG Chao-ming, QI Liang, ALLISON J E, MISRA A. Dislocation pile-ups at β_1 precipitate interfaces in Mg−rare earth (RE) alloys [J]. Materials Science and Engineering: A, 2019, 742: 278−286.

Y 元素对铸造 Mg−3Nd−0.2Zn−0.5Zr 合金显微组织演化及力学性能的影响

谢 赫[1]，吴国华[1]，张小龙[1]，李中权[2]，刘文才[1]，张 亮[1]，孙宝德[1]

1. 上海交通大学 材料科学与工程学院 轻合金精密成型国家工程研究中心&金属基复合材料国家重点实验室，上海 200240；
2. 上海航天精密机械研究所，上海 201600

摘　要：研究不同 Y 添加量(0、1.5%、3%和 4.5%，质量分数)对铸造 Mg−3Nd−0.2Zn−0.5Zr 合金显微组织演变及力学性能的影响规律。结果表明，随着 Y 含量的增加，铸态合金中主要的第二相由 $Mg_{12}Nd$ 型逐步转变为 $Mg_{24}Y_5$ 型。同时，固溶态合金中的 Zn−Zr 相的数量随着 Y 含量的增加逐渐减少。利用 HAADF-STEM 技术观察到峰时效状态下 Y 元素在球状柱面 β'相中显著富集。随着 Y 含量的增加，峰时效状态下合金中 β'的体积分数显著增大。由于 Y 元素的加入，β'相析出动力显著增大，进而使得合金强度得到显著提高。拉伸试验结果表明，当 Y 添加量为 4.5%(质量分数)时，在 200 和 225 ℃峰值时效条件下合金屈服强度增量分别为 88 和 61 MPa。

关键词：Mg−3Nd−0.2Zn−0.5Zr 合金；Y 合金化；时效硬化能力；显微组织演化；力学性能

(Edited by Wei-ping CHEN)